

# Accurate Measurements of Process Gas Flow with Laminar Flow Meters

Thiago Cobu

Instituto de Pesquisas Tecnológicas, Sao Paulo, Brazil

Tel: 55 11 3767 4604, Fax: 55 11 3766 3572, E-mail: thiagoc@ipt.br

Robert F. Berg, John D. Wright, and Michael R. Moldover

National Institute of Standards and Technology, Gaithersburg, MD, USA

Tel: 301-975-5937, Fax: 301-258-9201, E-mail: john.wright@nist.gov

**Abstract:** We calibrated three models of commercially-manufactured, laminar flow meters (LFMs) with nitrogen at four pressures (100 kPa, 200 kPa, 300 kPa, and 400 kPa) over a 10:1 flow range using NIST's primary flow standards and a physical model. Without additional calibration, each LFM was used to measure the flow of three process gases (Ar, He, and CO<sub>2</sub>) over the same pressure and flow ranges with a maximum error of only 0.5 %. The calibration and flow measurements used the gas-property data from NIST's database REFPROP 8.0 and a physical model for each meter that accounts for the viscous pressure drop, compressibility and non-ideal gas behavior, slip flow effects, kinetic energy effects, gas expansion effects, and thermal effects. The three LFMs have design differences that illustrate the dependence of the model corrections on LFM construction and the gas used. The LFM model improves results for the conditions tested by a factor of 4 over the flow coefficient and viscosity coefficient plots commonly used to present LFM calibration data.

**Keywords:** Laminar flow meter, gas species, gas properties, rate of rise, dynamic flow standard, gravimetric flow standard, process gases

## 1. Introduction

The users and manufacturers of flow meters for process gases often calibrate meters with one gas and use them to measure the flow of other gases. Below, we show that this can be done with a maximum error of only 0.5 % for 3 different, commercially-manufactured, laminar flow meters (LFMs) by using nitrogen for calibrations and the 3 gases Ar, He, and CO<sub>2</sub> as test gases. For each meter and gas, the data span the pressure range 100 kPa to 400 kPa and a 10:1 flow range. Our results rely on NIST's primary flow standards and the gas-property data in NIST's database REFPROP 8.0. [1] We interpreted the calibration data for each LFM using a physical model that accounted for the viscous pressure drop, compressibility and non-ideal gas behavior, slip flow effects, kinetic energy effects, gas expansion effects, and thermal effects.

In the near future, we hope to demonstrate that nitrogen calibrations can be used to measure the flow of additional process gases such as sulfur hexafluoride. The present measurements can be improved, particularly at low flows and pressures, by using better pressure instrumentation. At any particular Reynolds number, the present data for N<sub>2</sub>, Ar, and CO<sub>2</sub> are mutually consistent, generally within 0.2 %. However, the helium data differ by approximately 0.3 %. A fraction of this 0.3 % difference might result from an imperfection of REFPROP 8.0. However, the uncertainty of the viscosity of many reactive process gases is 0.5 % or larger. [2] For these gases, better flow measurements and/or better models for LFMs will have limited value.

Our objective, in common with that of previous authors, is to increase the accuracy of flow measurements made with commercially manufactured LFMs without requiring extensive, gas-specific calibrations. Typical calibrations of LFMs account for laminar flow viscous effects (the Hagen-Poiseuille equation) and for kinetic energy effects. Based on dimensional analysis, results are often displayed as a plot of the flow coefficient  $FC$  as a function of the viscosity coefficient  $VC$  [3,4] with the definitions:

$$FC \equiv \frac{L^3 (P_2 - P_1)}{\eta \dot{V}} \quad \text{and} \quad VC \equiv \frac{L^2 \rho (P_2 - P_1)}{\eta^2}. \quad (1)$$

Here  $L$  is the length of the laminar flow path,  $P_1$  and  $P_2$  are the upstream and downstream pressures,  $\eta$  and  $\rho$  are the gas viscosity and density, and  $\dot{V}$  is the volumetric flow.\* To the extent that the data collapse on a single curve, a plot of  $FC$  as a function of  $VC$  is a correlation that a user can represent with a convenient, analytic function. In the present work we achieved higher accuracy by using a more elaborate physical model that accounts for slip, gas expansion, and several smaller effects.

The starting point for our LFM models is the capillary model that Berg used to measure the viscosities of the gases He, N<sub>2</sub>, Ar, C<sub>3</sub>H<sub>6</sub>, and SF<sub>6</sub> with a  $k = 1$  uncertainty of 0.04 % [5]. Berg's capillary model accumulates the work of predecessors to include: geometric parameters (the length and the radius of the capillary), gas-dependent parameters, and a surface-dependent parameter. Commercially-manufactured LFMs have complex geometries that we model using the simple cross sections and lengths sketched in Table 1. For these simple shapes, we estimated all of the geometric parameters except for the smallest transverse dimension in each cross section that roughly corresponds to the radius of a capillary. In principle, one could fit this small dimension using a single calibration measurement, for example from the flow of nitrogen at ambient temperature and pressure, but in practice, we fit to the nitrogen data for all flows and pressures. From these one-parameter fits, we can predict the response of each LFM within 1.5 % for the three test gases over the full range of pressures and flows. Alternatively, we can replace the approximate, calculated values of certain LFM model parameters with values fitted to nitrogen calibration data spanning the complete range of pressure and flow. Then, we can predict the response of each of these LFMs within 0.5 %. This factor-of-3 improvement motivated us to present both the 1-parameter and multi-parameter results in the body of this paper.

## 2. Physical Model for the Laminar Flow Meters

The simplest model for a laminar flow meters is the Hagen-Poiseuille equation

$$\dot{m} = \frac{\pi \rho r^4 (P_1 - P_2)}{8 \eta L}, \quad (2)$$

which relates the mass flow rate of an incompressible fluid through a capillary of circular cross section to the density  $\rho$  and viscosity  $\eta$  of the fluid, the capillary radius  $r$  and length  $L$ , and the pressure drop  $P_1 - P_2$  along the capillary. The assumptions of the Hagen-Poiseuille equation are [6]:

1. the capillary is straight and has a uniform circular cross section
2. the fluid is incompressible and its density is constant
3. the fluid is Newtonian

4. the temperature of the fluid is constant and heat generation due to viscous dissipation is negligible
5. the flow is laminar and steady
6. there is no slip at the wall of the capillary

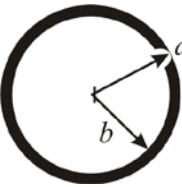
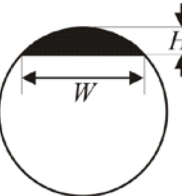
The first assumption is invalid when the flow meter has a noncircular cross section. Fortunately, hydrodynamic equations have been derived for a variety of cross sections; see, for example, Shah and London [7] or White [8]. The second assumption of incompressibility is of course invalid for gases, but combining the incompressible equation with the ideal gas law gives an expression that is simple and accurate to within a few percent for most LFMs.

Further improving the accuracy requires corrections for the following five effects:

- Density dependence of the gas viscosity and departures from the ideal gas law.
- Slip at the capillary wall, which increases the flow. This effect is proportional to the Knudsen number,  $Kn$ , which is the gas mean free path divided by a length that characterizes the capillary cross section.
- Gas expansion along the capillary, which increases the kinetic energy and decreases the flow.
- The increase of kinetic energy near the capillary entrance, which also decreases the flow. This correction is needed because the upstream pressure is measured by a tap located in a chamber before the capillary, in which the flow velocity is much smaller than in the capillary.
- The transverse temperature distribution in the fluid due to the imperfect cancellation of cooling due to gas expansion and viscous heating due to shearing.

The models used here include corrections for these effects. Two of the models are similar to previously published models [5,9], except they do not include a correction for centrifugal effects because the commercial LFMs had straight flow paths.

*Table 1. Cross section geometry (not to scale), full scale flow, and dimensions of the laminar flow meters. For each geometry, the dimension that was fitted to the data is underlined.*

Flow meter	Geometry	Flow Full Scale (scm)*	Dimensions
Circular		1000	$n = 12$ <u><math>r = 0.21 \text{ mm}</math></u> $L = 75 \text{ mm}$ $L/r = 350$
Annular		1000	$a = 3.947 \text{ mm}$ <u><math>a - b = 0.035 \text{ mm}</math></u> $L = 60 \text{ mm}$ $L/(a - b) = 1720$
Circular segment		100	<u><math>H = 0.089 \text{ mm}</math></u> $W = 1.2 \text{ mm}$ $L = 60 \text{ mm}$ $L/H = 674$

\* sccm = standard cubic centimeter per minute with reference conditions of 101.325 kPa and 0 °C.

Table 1 characterizes the three LFMs used in this study. The circular LFM is a bundle of 12 tubes with no flow passage in the interstitial spaces. The LFM with the annular cross section was constructed by centering a solid cylinder of radius  $b$  inside a hollow cylinder of a slightly larger diameter  $a$ . The circular segment LFM was constructed by placing a solid cylinder of diameter  $D$  with a small flat ground along its length inside a hollow cylinder of the same diameter. The resulting cross section is a shallow circular segment whose width  $W$  and maximum height  $H$  are related, in the limit of small  $W/D$ , by  $H = W^2/(2D)$ .

Equation 3 gives the model for mass flow for a single circular tube that accounts for the effects listed in Section 2 [5]:

$$\dot{m} = \dot{m}_0 \left[ 1 + g_{\text{virial}}(P_1, P_2) + 4K_{\text{slip}}Kn + \frac{K_{\text{ent}} + K_{\text{exit}}}{16} \frac{r}{L} Re + \left( \frac{K_{\text{exp}}}{8} + \frac{K_{\text{therm}}}{16} \right) \frac{r}{L} Re \ln \left( \frac{P_2}{P_1} \right) \right]. \quad (3)$$

The corresponding equations for the LFMs with annular and circular-segment cross sections have the same functional form with different geometric parameters. To emphasize this, we rewrite Eq. (3) in the generalized form

$$\dot{m} = \dot{m}_0 \left[ 1 + g_{\text{virial}}(P_1, P_2) + \alpha K_{\text{slip}}Kn + \beta(K_{\text{ent}} + K_{\text{exit}})Re + \gamma(2K_{\text{exp}} + K_{\text{therm}})Re \ln \left( \frac{P_2}{P_1} \right) \right] \quad (4)$$

where the geometrical parameters  $\alpha$ ,  $\beta$ , and  $\gamma$  for the 3 LFMs are listed in Table 2. Similarly, the uncorrected mass flow for a circular cross section is generalized as

$$\dot{m}_0 = \frac{\pi \mathcal{M} r^4 (P_1^2 - P_2^2)}{16\eta(T, 0)LRT} = \delta \frac{\mathcal{M} (P_1^2 - P_2^2)}{\eta(T, 0)LRT}. \quad (5)$$

where the geometrical parameter  $\delta$  in the generalized version is also listed in Table 2. In Eq. (5),  $r$  and  $L$  are the LFM radius and length,  $R$  is the universal gas constant,  $T$  is the temperature,  $\mathcal{M}$  is the molar mass, and  $\eta(T, 0)$  is the gas viscosity evaluated at temperature  $T$  in the limit of zero pressure.

Table 2. The parameters of the generalized LFM model (Equations 4, 5, 6, and 8) for each tube geometry.

	$\alpha$	$\beta$	$\gamma$	$\delta$	$P_w$	$D_h$
Circular	4	$\frac{1}{16} \frac{r}{L}$	$\frac{1}{16} \frac{r}{L}$	$\frac{\pi r^4}{16}$	$2\pi r$	$2r$
Annular	6	$\frac{1}{12} \frac{(a-b)}{L}$	$\frac{1}{20} \frac{(a-b)}{L}$	$\frac{\pi a(a-b)^3}{6}$	$2\pi(a+b)$	$2(a-b)$
Circular Segment	4	$\frac{1}{24} \frac{H}{L}$	$\frac{9}{140} \frac{H}{L}$	$\frac{WH^3}{96}$	$2W$	$H$

The five corrections in Eq. (4) depend on the Reynolds number  $Re$ , the Knudsen number  $Kn$ , and the function  $g_{\text{virial}}$ , which corrects for the density dependence of the gas viscosity and departures from the ideal gas law. In previous work [5, 9], the values of  $K_{\text{slip}}$ ,  $K_{\text{ent}}$ ,  $K_{\text{exit}}$ ,  $K_{\text{exp}}$  and  $K_{\text{therm}}$  were determined analytically, computationally, or experimentally. As described in Appendix A, we

used such estimates as a starting point (“assumed  $K$  values”). We also adjusted the  $K$  values based on the nitrogen calibration data (“fitted  $K$  values”). The LFM models were tested with both sets of  $K$  values using flow data for the three other gases: Ar, He, and CO<sub>2</sub>.

For all three LFM geometries, the length scale used in the Reynolds number is the hydraulic diameter,  $D_h = 4A/P_w$ , where  $A$  is the flow area and  $P_w$  is the “wetted perimeter” of the flow path. The Reynolds number for an LFM is

$$Re = \frac{4\dot{m}}{P_w \eta(T, \bar{P})}, \quad (6)$$

where values of the geometric parameter  $P_w$  and  $D_h$  for each cross section are listed in Table 2. In Eq. (6),  $\eta(T, \bar{P})$  is the viscosity evaluated at the pressure averaged along the length of the capillary:

$$\bar{P} \cong \frac{2(P_1^3 - P_2^3)}{3(P_1^2 - P_2^2)}. \quad (7)$$

Note that the equations for mass flow and Reynolds number given above are for a single flow path, and the model flow for a single tube must be multiplied by the total number of tubes, e.g.  $n = 12$  for the circular LFM shown in Table 1.

The Knudsen number is defined as

$$Kn = \frac{\lambda_{1/2}}{D_h / 2}, \quad (8)$$

where

$$\lambda_{1/2} = \left( \frac{2RT}{\mathcal{M}} \right)^{1/2} \frac{\eta(T, P_{1/2})}{P_{1/2}} \quad (9)$$

is the mean free path evaluated at  $P_{1/2} \equiv (P_1 + P_2) / 2$ .

The expressions for the annular and circular segment models are approximations that are valid in the respective limits  $H \ll W$  and  $(a - b) \ll a$ . For the annular model, the exact solution for  $\delta$  is [7, 8]

$$\delta = \frac{\pi}{8} \left[ a^4 - b^4 - \frac{(a^2 - b^2)^2}{\ln(a/b)} \right], \quad (10)$$

which simplifies to the expression listed in Table 2 that shows that the flow depends on the cube of the gap between the cylinders. Appendix B explains the derivation of the circular segment model.

### 3. Description of Measurements

A pressure regulator and mass flow controller were used to set the flow of gas at the laminar flow meter. A back-pressure regulator or a throttling valve was used to maintain a nominal pressure at the exit of the LFM despite downstream pressure changes, e.g. due to the filling of the collection tank. With this equipment, each LFM was tested at flows of 10 %, 25 %, 50 %, 75 %, and 100 % of full scale and the nominal pressures at the LFM exit were 100 kPa, 200, kPa, 300 kPa, and 400 kPa. This arrangement gave at least 20 combinations of flow and pressure for each flow

meter and each gas. The gases used were nitrogen, argon, helium, and carbon dioxide. The data plotted herein are averages of 10 or more individual flow measurements made at each set point condition.

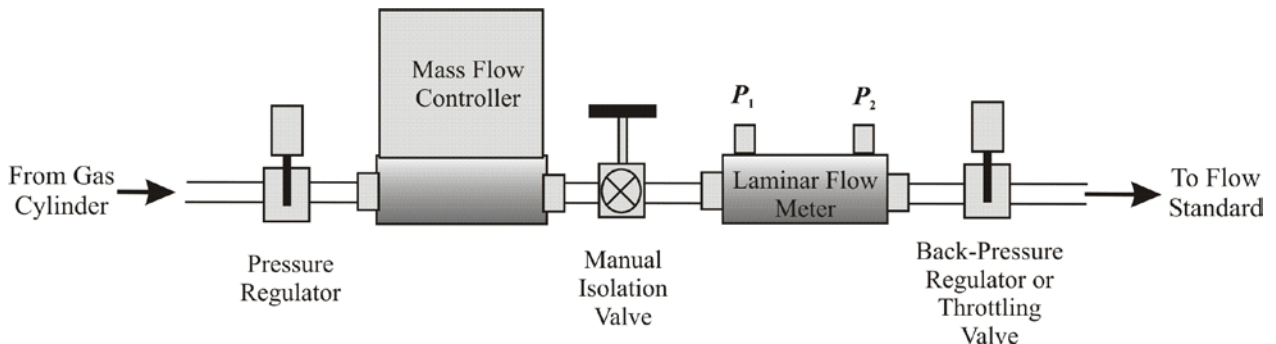


Figure 1. Schematic of the test arrangement to calibrate the laminar flow meters against the *PVTt* and *RoR* flow standards.

For the circular segment LFM and the annular LFM,  $P_1$  and  $P_2$  were measured with two absolute pressure sensors with a full scale of 550 kPa. The differential pressures ranged from 2 kPa to 63 kPa. Periodic taring of the two sensors kept differential pressure standard uncertainties within 5 Pa, i.e. 0.25 %\* of the minimum differential pressure.

For the circular LFM,  $P_1$  was measured with a 1400 kPa full scale sensor (0.02 % uncertainty). The differential pressure  $P_1 - P_2$  ranged from 0.1 kPa to 2.6 kPa, and it was measured with a 10 kPa full scale sensor with standard uncertainty of 1 Pa, i.e. 1 % of the minimum differential pressure. LFM gas temperature (0.04 % uncertainty) was measured by placing sensors in good contact with the LFM body.

Three flow standards were used to calibrate the LFMs and to evaluate the LFM physical model:

1) *PVTt*: The 34 L *PVTt* standard determined the mass of gas accumulated in a collection tank over a measured period of time. Details about this standard and its uncertainty of 0.013 % can be found in reference [10].

2) *Rate-of-Rise*: At 10 sccm, it takes 57 h to make a single *PVTt* flow measurement that fills the 34 L collection tank from vacuum to 100 kPa. Fortunately, the *Rate-of-Rise* technique allows the same tank and instrumentation to be used more efficiently. This method acquires time-stamped pressure and temperature values for the gas in the collection tank as the tank is filling. The pressure and temperature are used to calculate the density of gas. The mass of gas at each time step is obtained by multiplying the density by the collection volume. At each time  $t_i$ , the slope of the accumulated mass with respect to time is the mass flow rate, i.e.:

$$\dot{m} = \frac{d}{dt} [V\rho(P, T)] \cong V \left[ \frac{\rho(P_{i+1}, T_{i+1}) - \rho(P_i, T_i)}{t_{i+1} - t_i} \right]. \quad (11)$$

Our analysis for this technique gives a standard uncertainty of 0.027 %.

\* Uncertainties herein are standard,  $k = 1$  with a 67 % confidence level unless otherwise stated.

3) Dynamic Gravimetric: A commercial dynamic gravimetric flow standard was used to measure the mass of a pressurized gas cylinder as a function of time while discharging through the LFM. The standard uncertainty of the gravimetric flow standard is 0.05 % [11].

Comparisons between the three flow standards agreed within 0.05 %.

#### 4. Results and Discussion

For each LFM, the model was fit to the data in two ways. The first way assumed that the values of  $K_{\text{slip}}$ ,  $K_{\text{ent}}$ ,  $K_{\text{exit}}$ , and  $K_{\text{exp}}$  had the values indicated in Table 3. As explained in Appendix A, each value was based on either a calculation or a simple physical assumption, so that the model's only free parameter was the transverse (smallest) dimension underlined in Table 1 ( $r$ ,  $a$ - $b$ , or  $H$ ). The second way added one or two free parameters by allowing  $K_{\text{ent}}$ ,  $K_{\text{exit}}$ , and  $K_{\text{exp}}$  to vary from their assumed values. For both ways, the fitted coefficients given in Table 4 and the transverse dimensions listed in Table 1 were determined by minimizing the differences between the LFM model and reference flow measurements in nitrogen.

Table 3. When the model's only free parameter was the LFM transverse dimension (underlined in Table 1), these values were assumed for the model coefficients.

	$K_{\text{slip}}$	$K_{\text{ent}}$	$K_{\text{exit}}$	$K_{\text{exp}}$
circle [5]	1	-1.14	0	1
annulus [9]	1	-0.90	0	1
circle segment	1	-1.00	0	1

Table 4. When  $K_{\text{ent}}$ ,  $K_{\text{exit}}$ , and  $K_{\text{exp}}$  were used as free parameters, the underlined values were obtained.

	$K_{\text{slip}}$	$K_{\text{ent}}$	$K_{\text{exit}}$	$K_{\text{exp}}$
circle	1	<u>-1.30</u>	0	1
annulus	1	-0.90	<u>0.60</u>	1
circle segment	1	-1.00	<u>0.23</u>	<u>0.55</u>

Figures 2, 4, and 6 plot the ratios of the modeled flow to the reference flow versus the Reynolds number. Each plot includes all of the flow and pressure combinations for all four gases. The left half is a plot using the assumed coefficients listed in Table 3. The right half shows the results when the coefficients underlined in Table 4 were allowed to be free parameters.



Figure 2. Flow ratio versus Reynolds number for the circular LFM for literature and fitted  $K$  values.

Figure 2 shows the results for the circular LFM, and Figure 3 demonstrates the significance of the model's correction terms. The corrections are plotted versus flow for low pressure helium and high pressure carbon dioxide. The entrance correction is as large as 11 % due to the small aspect ratio ( $L/r = 357$ ). The largest virial correction, 2 %, occurred for carbon dioxide at 400 kPa.

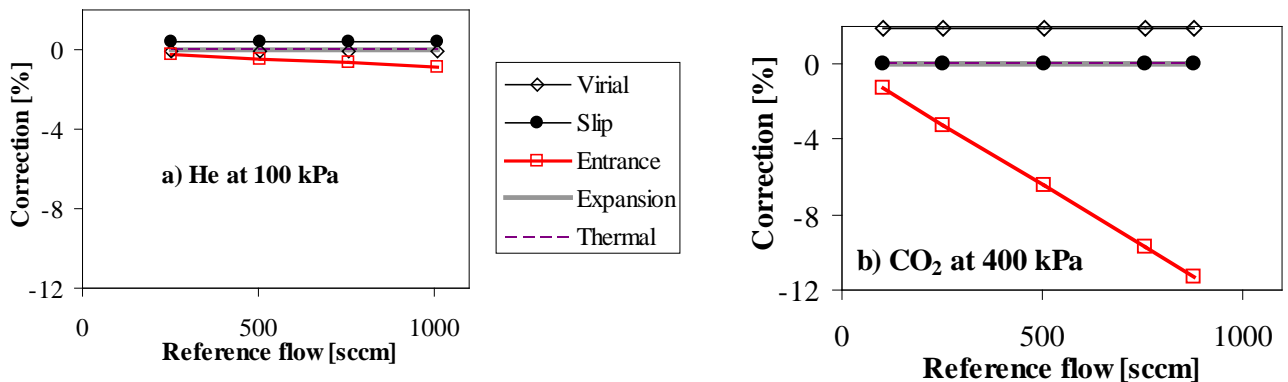


Figure 3. Corrections applied for the circular LFM for a) helium at  $P_2 \approx 100$  kPa and b) carbon dioxide at  $P_2 \approx 400$  kPa.

Figure 2 shows that using the expected value for the entrance correction coefficient,  $K_{\text{ent}} = -1.14$ , caused deviations of the model that depend only on Reynolds number. The expected value of  $K_{\text{ent}}$  had been calculated for a single capillary, so we speculated that the deviations were caused by the collective effect of the 12 capillaries on the flow field near the capillary entrances. In that spirit, we allowed  $K_{\text{ent}}$  to be a free parameter. The right side of Figure 2 shows that the value  $K_{\text{ent}} = -1.30$  significantly reduced the deviations. (The curvature of the deviations could not be reduced because the entrance correction term in Eq. (3) is linear in  $Re$ .)

Figure 4 shows the results for the annular LFM. With only one free parameter, the gap dimension  $a-b$ , the deviations were less than 0.5 %. The right side of Figure 4 shows that allowing  $K_{\text{exit}}$  to be a free parameter reduced the deviations significantly. As explained in Appendix A, the geometry of the duct suggests that a nonzero value of  $K_{\text{exit}}$  is reasonable, and its fitted value falls in the physically allowed range  $0 < K_{\text{exit}} < |K_{\text{ent}}|$ .

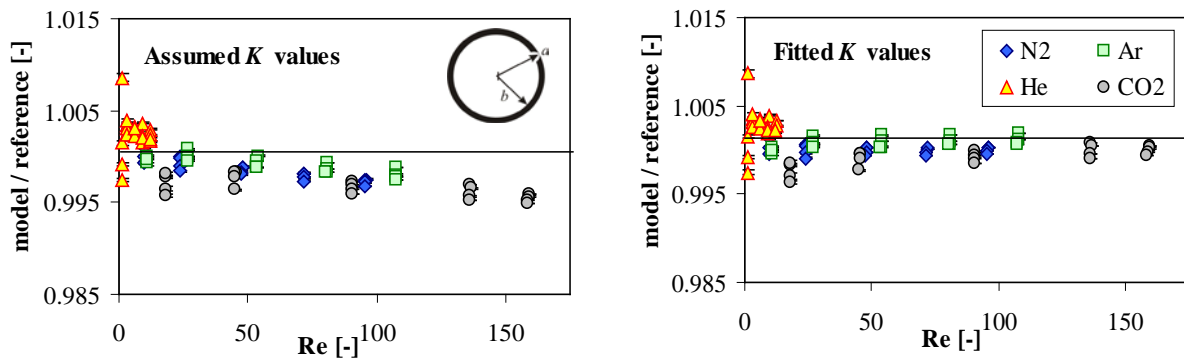


Figure 4. Flow ratio versus Reynolds number for the annular LFM.

Figure 5 shows the model corrections for nitrogen at 400 kPa and helium at 100 kPa. The relatively large aspect ratio,  $L/(a-b) = 1720$ , yields small entrance and exit corrections ( $< 0.3\%$ ). However, the relatively small transverse dimension ( $a-b$ ) leads to a large Knudsen number, particularly for low pressure helium, and it gives slip corrections as large as 3.5%. At fixed exit pressure, the slip correction decreases with flow because the average pressure increases, which shortens the mean free path.

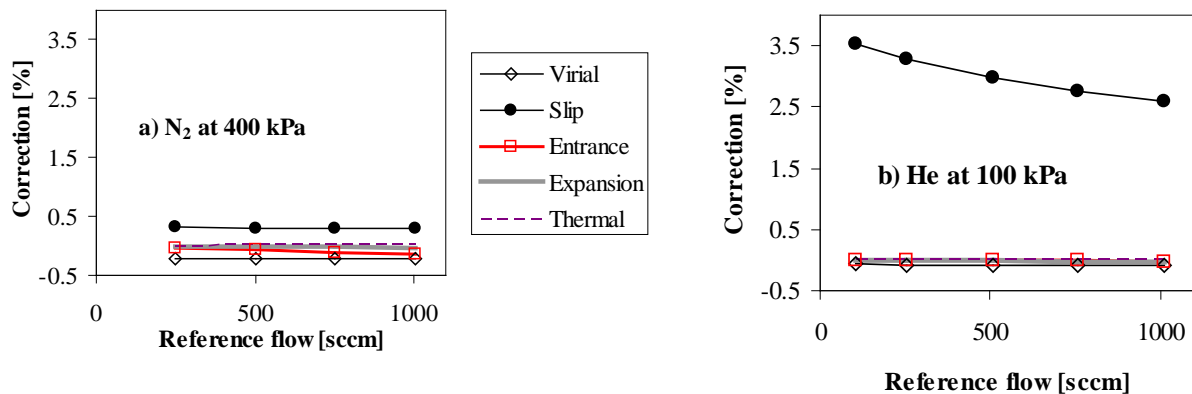


Figure 5. Corrections applied for the annular LFM for a) nitrogen at  $P_2 \approx 400$  kPa and b) helium at  $P_2 \approx 100$  kPa.

Figure 6 shows the results for the circular segment LFM. As with the annular LFM, allowing  $K_{\text{exit}}$  to be a free parameter yielded a plausible value for  $K_{\text{exit}}$  and corrected much of the Reynolds number dependence seen on the left side of Figure 6. However, adjusting  $K_{\text{exit}}$  could not remove the pressure dependence seen at low pressures and high  $Re$  because the associated correction term depends only on  $Re$ . In contrast, the expansion correction term depends on the pressure ratio  $P_2/P_1$  as well as  $Re$ , and the right side of Figure 6 shows that reducing  $K_{\text{exp}}$  from 1 to 0.55 significantly reduced the pressure dependence. We have no explanation for why the fitted value should differ from the value  $K_{\text{exp}} = 1$  implied by the calculation in Appendix C.

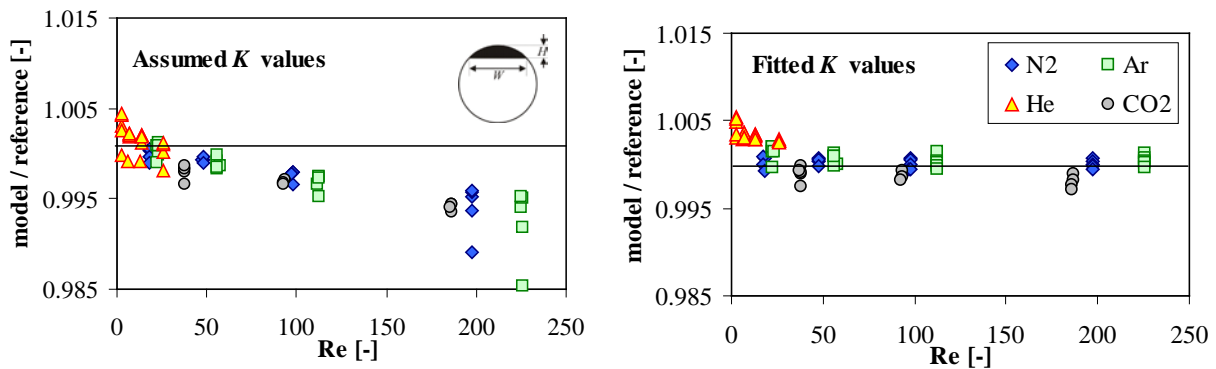


Figure 6. Flow ratio versus Reynolds number for the circular segment LFM.

Figure 7 shows the model corrections for nitrogen at two exit pressures. The expansion correction is more significant at the lower pressure because, as the exit pressure increases,  $P_2 \rightarrow P_1$  and the  $\ln(P_2/P_1)$  dependence of this correction term approaches zero. At the largest flow, entrance and exit corrections are approximately twice as large as any other correction.

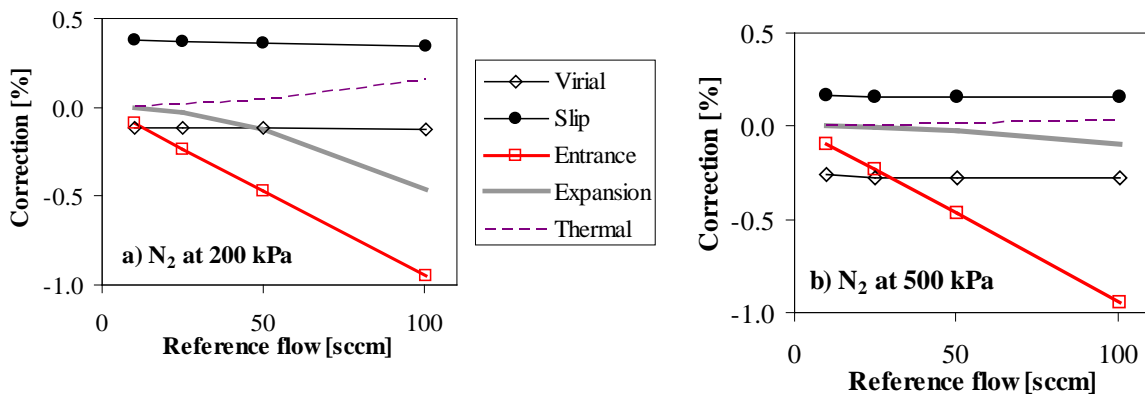


Figure 7. Corrections applied for the circular segment LFM for nitrogen at a)  $P_2 \approx 200$  kPa and b)  $P_2 \approx 500$  kPa.

The experimental results in this paper are based on measurements of absolute pressure, differential pressure, temperature, and mass flow, plus REFPROP values of compressibility, density, and viscosity. The most significant associated uncertainties are for the measurements of differential pressure at low flows (10 % of LFM full scale) and for the REFPROP values of viscosity. There are opportunities for improving the measurements by using better pressure instrumentation. The uncertainty of the REFPROP viscosity values is estimated to be 0.5 % at  $k = 2$ , or 95 % confidence level [12]. At any particular Reynolds number, the agreement between nitrogen, argon, and carbon dioxide is better than that, generally  $< 0.2$  %. However, the helium data are approximately 0.3 % higher for all three LFMs.

## 5. Summary

Equation (4) gives a physical model for the laminar flow meter based on the Hagen-Poiseuille equation, generalized for various flow path geometries, with corrections for non-ideal gas effects,

slip flow, end effects, gas expansion through the meter, and thermal effects. For three commercially produced LFMs, the coefficients of the LFM model were established based on literature values and calibrations of the LFMs in nitrogen. The LFMs were also calibrated in argon, helium, and carbon dioxide for a range of flows (10% to 100 % of full scale flow) and pressures (100 kPa to 400 kPa). The LFM model was evaluated by plotting the ratio of the model predicted flows to flows from reference flow standards with uncertainty  $< 0.1\%$ . The NIST properties database REFPROP was used for density and viscosity values. The spread of the results for all three LFM geometries was  $< \pm 1.5\%$  when the assumed values of  $K$  were used. When the  $K$  values were based on fits to nitrogen data, the model gave flows within  $\pm 0.5\%$  of the flow standards for the 4 gases tested.

It is clear from the circular LFM results that the current model does not capture all of the physical phenomena when kinetic energy effects are large, i.e. when  $L/r$  is small. The pressure dependence observed for the circular segment LFM, which we corrected using  $K_{\text{exp}}$ , also requires explanation and may be due to missing physics in the present LFM model.

Figure 8 shows the results when fits to the viscosity and flow coefficients [defined in Eq. (1)] are applied to the data collected with two of the LFMs. For the circular segment LFM, the neglect of slip for the helium data at 100 kPa causes errors up to 1.5 %. Residuals due to slip effects in the annular LFM (not shown) are as large as 2.7 %. The large entrance and exit effects for the circular LFM are accounted for in the  $FC$  versus  $VC$  fits, but the neglect of other corrections leads to residuals up to 1.2 % (see right side of Figure 8).

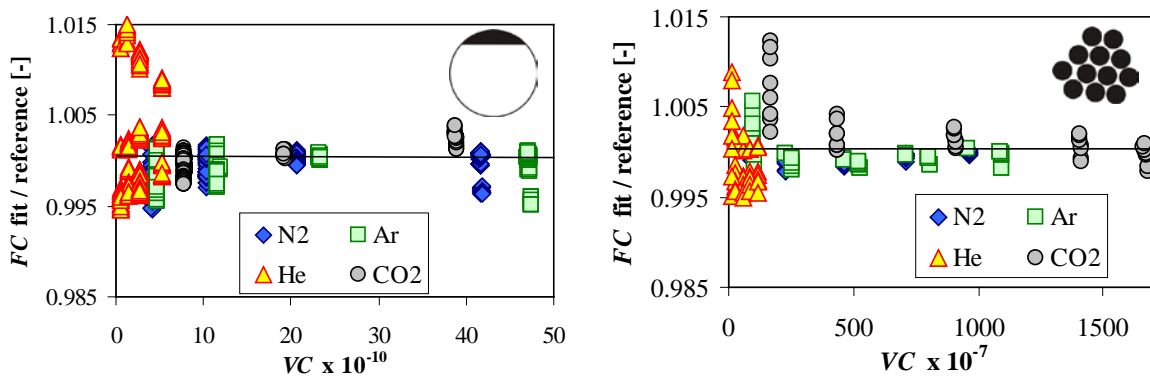


Figure 8. Flow ratios when commonly used flow coefficient versus viscosity coefficient plots are applied to two of the three LFMs. Residuals are as much as 4 times worse than the LFM model.

The results are instructive to those who use LFMs with multiple gases, and it motivates us to move beyond  $FC$  versus  $VC$  fits. We anticipate that laboratories that calibrate LFMs will design data collection protocols optimized to determine the LFM model parameters, i.e. transverse dimension,  $K_{\text{ent}} + K_{\text{exit}}$ , and  $K_{\text{exp}}$ . This protocol is likely to be one gas, tested at different values of  $P_{1/2}$ .

### Appendix A: Constants in the Flow Models

The constant  $K_{\text{slip}}$  is a measure of momentum accommodation, and previous experience [9,13] found that  $K_{\text{slip}} = 1.00$  for impedances with metal surfaces. The only exception seen previously was a value as large as 1.2 for helium flowing through a quartz capillary [5]. The values of  $K_{\text{ent}}$

and  $K_{\text{exp}}$  expected for the circle and the annulus were obtained from [5] and [9]. Appendix C gives the derivation of these constants for the circular segment.

The parameter  $K_{\text{exit}}$  describes the recovery of pressure from the kinetic energy of fluid leaving the exit of the LFM. For the circular LFM,  $K_{\text{exit}} \cong 0$  was expected because the exiting fluid is dissipated as heat when it jets out of a small duct into a much larger chamber. (See the discussion in [2?]).



Figure 9. Longitudinal cross section of the annular LFM. The gas flowed through the small gap between concentric cylinders. The tapered end of the inner cylinder reduced turbulence in the gas exiting the gap. The inner cylinder used in the circular segment LFM cylinder had a similar taper.

However, dissipation at the exit seemed to be smaller for the annular and circular segment LFMs. As indicated by Figure 9, the duct for the annular LFM was defined by a central cylinder with tapered ends. The resulting smooth opening of the duct likely reduced jetting and dissipation in the exit chamber and thereby required the use of  $K_{\text{exit}} \neq 0$  as a second free parameter. The circular segment LFM had a duct with a similar taper, but its value of  $K_{\text{exit}}$  had a smaller magnitude. Perhaps this occurred because flow exiting a circular segment is more likely to jet than flow exiting an annulus.

The value of  $K_{\text{therm}}$  depends on both the gas and the shape of the LFM's cross section. Appendix A of [5] gives the general expression for a circular cross section,

$$K_{\text{therm}} = - \left[ 1 + \frac{1}{3} \left( \frac{T}{\eta} \frac{\partial \eta}{\partial T} \right) \right] \frac{R\eta}{\mathcal{M}\kappa}, \quad (12)$$

where  $\mathcal{M}$  and  $\kappa$  are respectively the molar mass and thermal conductivity of the gas. The nature of the thermal correction suggests that the value of  $K_{\text{therm}}$  is insensitive to the shape of the LFM's cross section. We therefore assigned the value of  $K_{\text{therm}}$  for the circle to that for the other two shapes, and we assumed the thermal correction was half that of the expansion correction, as was the case for the circular cross section.

Table 5. Values of  $K_{\text{therm}}$ .

Gas	$K_{\text{therm}}$
He	-0.33
N <sub>2</sub>	-0.26
Ar	-0.34
CO <sub>2</sub>	-0.22

## Appendix B: The Function $g_{\text{virial}}$

The function  $g_{\text{virial}}$ , which accounts for the density dependence of the gas viscosity and departures from the ideal gas law, can be derived as follows. For a circular cross section the differential form of Poiseuille's Law is

$$dP = -\frac{8\eta(T,P)Q(T,P)}{\pi r^4} dz, \quad (13)$$

where  $Q$  is the volume flow and  $z$  is the length along the capillary. For an ideal gas whose viscosity is pressure-independent, integrating Eq. (13) gives the uncorrected flow,  $\dot{m}_0$  of Eq. (5). Integrating Eq. (13) for a nonideal gas and dividing by  $\dot{m}_0$  gives the following ratio.

$$1 + g_{\text{virial}}(P_1, P_2) = \frac{\int_{P_1}^{P_2} [\rho(T,P)/\eta(T,P)] dP}{\int_{P_1}^{P_2} [\rho_{\text{ideal}}(T,P)/\eta(T,0)] dP} = \frac{2}{(P_1^2 - P_2^2)} \int_{P_1}^{P_2} \frac{P/Z(T,P)}{\eta(T,P)/\eta(T,0)} dP \quad (14)$$

For a gas that is nearly ideal, this integral can be approximated by a function of the virial coefficients for pressure and viscosity [5]. In this work we instead obtained values of the integrand from REFPROP and calculated the integral numerically. Simpson's rule, which required property values at only three pressures,  $P_1$ ,  $P_{1/2}$ , and  $P_2$ , was sufficiently accurate, and it was easy to implement in a spreadsheet:

$$1 + g_{\text{virial}}(P_1, P_2) = \frac{1}{2P_{1/2}} \left[ \frac{1}{3} \frac{P_1/Z(T, P_1)}{\eta(T, P_1)/\eta(T, 0)} + \frac{4}{3} \frac{P_{1/2}/Z(T, P_{1/2})}{\eta(T, P_{1/2})/\eta(T, 0)} + \frac{1}{3} \frac{P_2/Z(T, P_2)}{\eta(T, P_2)/\eta(T, 0)} \right] \quad (15)$$

### Appendix C: Derivation of the Flow Model for the Circular segment

Laminar flow through a duct whose cross section is a circular segment has been calculated previously by numerical means [7]. Here we approximated the circular segment by a very obtuse isosceles triangle, which gave two advantages. First, as shown in Figure 10, the triangle could be further approximated by many pairs of parallel plates, which eased the calculations of the slip, entrance, and expansion corrections. Second, the parallel-plate calculation could be checked against an exact solution. Both calculations are described below, followed by the adjustment for compressible flow. The last three calculations derive the corrections for slip, flow near the entrance, and expansion.

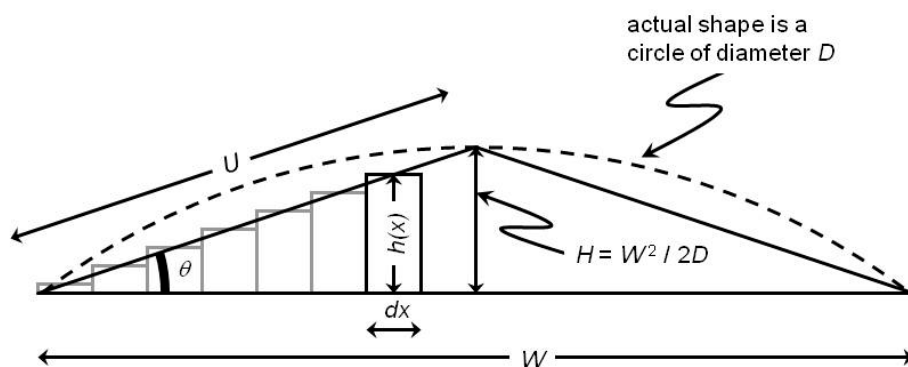


Figure 10. The flow through the very obtuse triangle is approximately the sum of a set of flows through parallel plates.

### Incompressible Flow: Parallel-Plate Approximation

Figure 3 approximates the obtuse triangle as many pairs of parallel plates of height  $h(x)$  and differential width  $dx$ , where  $x$  is the distance along the triangle base from the corner to the

middle. To simplify the derivation, assume for now that the fluid is incompressible. The volume flow through the rectangle defined by one pair of plates is

$$dQ = \frac{h^3 dx}{12\eta L}. \quad (16)$$

and the total volume flow through the entire triangle is

$$\begin{aligned} Q_0 &= 2 \left( \frac{P_1 - P_2}{12\eta L} \right) \int_0^{W/2} h^3 dx = \left( \frac{P_1 - P_2}{6\eta L} \right) \sin^3 \theta \int_0^{W/2} x^3 dx \\ &\cong \left( \frac{P_1 - P_2}{6\eta L} \right) \left( \frac{2H}{W} \right)^{3/2} \frac{(W/2)^4}{4} = \left( \frac{P_1 - P_2}{\eta L} \right) \frac{WH^3}{48} \end{aligned} \quad (17)$$

### Incompressible Flow: Exact Solution

This parallel-plate calculation was checked against a solution that combined analytical and numerical results for incompressible Poiseuille flow through a duct of triangular cross section and length  $L$ . Mortensen et al. [14] found that the volume flow is

$$Q_0 = \frac{(P_1 - P_2) A^2}{\eta L \alpha_D}, \quad (18)$$

where  $A$  is the area of the triangle and  $\alpha$  is a geometric factor that characterizes the effective hydraulic radius. Using Mortensen et al.'s result for  $\alpha_D$  with a very obtuse isosceles triangle with sides  $(U, U, W)$ , as shown in Figure 10, yields

$$Q_0 \cong \left( \frac{P_1 - P_2}{\eta L} \right) \frac{WH^3}{(800/17)}. \quad (19)$$

Eq. (19) validates the accuracy of the integral calculation of Eq. (17) because the two results disagree by a factor of only 51/50.

### Compressible Flow

Accounting for the gas's compressibility amounts to multiplying Eq. (17) by a factor of  $(P_1 + P_2) / (2RT)$  [5], yielding

$$\dot{m}_0 = \frac{\mathcal{M}WH^3 (P_1^2 - P_2^2)}{96\eta(T, 0) LRT}. \quad (20)$$

### Slip Correction

Adding a slip correction to the model requires changing the argument of the integral in the first line of Eq. (17) from  $h^3$  to  $h^3(1 + 6\lambda/h)$ . The factor of 6 is the value appropriate for flow through parallel planes [9]. The relative correction for slip is then

$$\begin{aligned} \frac{\Delta \dot{m}_{\text{slip}}}{\dot{m}_0} &= \frac{\int_0^{W/2} h^3 (1 + 6\lambda/h) dx}{\int_0^{W/2} h^3 dx} - 1 = \frac{6\lambda \int h^2 dx}{\int h^3 dx} \\ &= \frac{6\lambda/3}{(W/2)\sin\theta/4} \cong 4 \frac{\lambda}{H/2} \end{aligned} \quad (21)$$

### Entrance Correction

The kinetic energy change near the entrance causes a pressure drop of

$$\Delta P_1 = K_{\text{ent}} \rho_1 v_1^2 = K_{\text{ent}} \rho_1 \left( \frac{Q_1}{A} \right)^2, \quad (22)$$

where  $\rho_1$  and  $v_1 = Q_1/A$  are respectively the density and average velocity at the entrance, and

$$Q_1 = \frac{\dot{m}_0}{\rho_1} = \frac{WH^3(P_1^2 - P_2^2)}{96\eta(T,0)LP_1} \quad (23)$$

is the uncorrected volume flow at the entrance. The relative change of flow due to  $\Delta P_1$  is

$$\frac{\Delta \dot{m}_{\text{ent}}}{\dot{m}_0} = \frac{(P_1 + \Delta P_1)^2 - P_2^2}{P_1^2 - P_2^2} - 1 \cong \frac{2P_1 \Delta P_1}{P_1^2 - P_2^2}. \quad (24)$$

Substituting Eqs. (22) and (23) into Eq (24), using the area  $A = WH/2$ , and defining  $Re$  from Eq. (6) yields

$$\frac{\Delta \dot{m}_{\text{ent}}}{\dot{m}_0} = \frac{2P_1}{P_1^2 - P_2^2} K_{\text{ent}} \rho_1 \left( \frac{Q_1}{A} \right)^2 = \frac{K_{\text{ent}}}{24} \left( \frac{H}{L} \right) Re. \quad (25)$$

This expression is analogous to the entrance corrections for the circle and the annulus, for which  $K_{\text{ent}} = -1.14$  and  $-0.9$  respectively. Due to the similarity of  $K_{\text{ent}}$  for those very different cross sections and the intermediate aspect ratio of the circular segment, we assumed that  $K_{\text{ent}} = 1.0 \pm 0.1$  for the circular segment.

### Expansion Correction

Adding an expansion correction to the model requires using the expansion correction for the rectangular duct [9] to modify the argument of the integral in the first line of Eq. (17). The relative correction for expansion is then

$$\frac{\Delta \dot{m}_{\text{exp}}}{\dot{m}_0} = \frac{\int_0^{W/2} h^3 \left\{ 1 + \left( K_{\text{expRectangle}} / 5 \right) \left[ h / (2L) \right] Re_{\text{local}}(x) \ln(P_2 / P_1) \right\} dx}{\int_0^{W/2} h^3 dx} - 1, \quad (26)$$

where  $K_{\text{expRectangle}} = 9/7$  is the parallel-plate value for  $K_{\text{exp}}$  [9]. Using Eqs. (3), (4), and (9) of [9] gives an expression for the local Reynolds number:

$$\frac{Re_{\text{local}}(x)}{Re} = 2 \left[ \frac{h(x)}{H} \right]^3, \quad (27)$$

where  $Re_{\text{local}}(x)$  is the Reynolds number for a thin rectangle as defined by Eq. (9) of [9]. Using Eq. (27) in Eq. (26) gives

$$\begin{aligned} \frac{\Delta \dot{m}_{\text{exp}}}{\dot{m}_0} &= \frac{K_{\text{expRect}}}{5LH^3} \ln \left( \frac{P_2}{P_1} \right) Re \sin^4(\theta) \frac{\int_0^{W/2} x^7 dx}{\int_0^{W/2} x^3 dx} \cong \frac{(9/7)}{5LH^3} \ln \left( \frac{P_2}{P_1} \right) Re \left( \frac{2H}{W} \right)^4 \frac{1}{2} \left( \frac{W}{2} \right)^4 \\ &= \frac{9}{70} \left( \frac{H}{L} \right) \ln \left( \frac{P_2}{P_1} \right) Re \end{aligned} \quad (28)$$

### References

- [1] Lemmon, E. W., McLinden, M. O., and Huber, M. L., "Refprop 23: Reference Fluid Thermodynamic and Transport Properties," *NIST Standard Reference Database 23*, Version 8.0, National Institute of Standards and Technology, Boulder, CO, April, 2007.
- [2] Hurly, J. J., Gillis, K. A., Mehl, J. B., and Moldover, M. R., *The Viscosity of Seven Gases Measured with a Greenspan Viscometer*, International Journal of Thermophysics, 24, 6, pp. 1441 to 1474, November, 2004.

- 
- [ 3 ] Todd, D. A., *Laminar Flow Elements in Flow Measurement: Practical Guides for Measurement and Control*, 2<sup>nd</sup> edition, D. W. Spitzer editor, The Instrumentation, Systems, and Automation Society, Research Triangle Park, North Carolina, 205–239. 2001.
- [4] Wright, J. D., *The Long Term Calibration Stability of Critical Flow Nozzles and Laminar Flow Meters*, National Conference of Standards Laboratories Conference Proceedings, Albuquerque, New Mexico, 443–462, 1998.
- [5] Berg, R. F., *Simple Flow Meter and Viscometer of High Accuracy for Gases*, *Metrologia*, 42, pp. 11-23, 2005. Erratum **43**, p. 183, 2006.
- [ 6 ] Kawata, M., Murase, K., Nagashima, A., and Yoshida, K., *Capillary Viscometers, Measurement of the Transport Properties of Fluids* ed. W. A. Wakeham *et al* (Oxford: Blackwell), 1991.
- [7] Shah, R. K. and London, A. L., Laminar Flow Forced Convection in Ducts, in *Advances in Heat Transfer*, T. F. Irvine and J. P. Hartnett editors, Academic Press, 1978,
- [8] White, F. M., Viscous Fluid Flow, 2nd edition, McGraw Hill, 1991.
- [9] Berg, R. F. and Tison, S. A., *Laminar Flow of Four Gases through a Helical Rectangular Duct*, *AIChE Journal* 47, 2, pp. 263 – 270, 2001.
- [10] Wright, J. D. and Johnson, A. N., *NIST Lowers Gas Flow Uncertainties to 0.025 % or Less*, *NCSL International Measure*, **5**, pp. 30 to 39, March, 2010.
- [11] Bair, M. and Rombouts, C., *Typical Measurement Uncertainty in Gas Flow Measured by GFS2102 Gravimetric Flow Standard*, Technical Note 6050TN09, DH Instruments, May 31, 2006.
- [12] Wright, J. D., *Properties for Accurate Gas Flow Measurements*, FLOMEKO, Taipei, Taiwan, October 13 – 15, 2010.
- [13] May, E. F., Berg, R. F., and Moldover, M. R., *Reference viscosities of H<sub>2</sub>, CH<sub>4</sub>, Ar and Xe at low densities*, *Int J. Thermophys.* **28**, pp. 1085 to 1110, 2007.
- [14] Mortensen, N. A., Okkels, F., and Bruus, H. “*Reexamination of Hagen-Poiseuille Flow: Shape Dependence of the Hydraulic Resistance in Microchannels*”, *Phys. Rev. E* 71, 057301, 2005. In their Eq. (16), the factor of 8 is incorrect and should be 81/2.